Journal of Applied Physics

RESEARCH ARTICLE | MARCH 03 2026

Optical and electrical signatures of charge trapping in hybrid perovskite $MAPbBr_3$ single crystals

Frida Marie Lund Jeppesen ; Josipa Šćurla ; Milica Vasiljević ; Endre Horváth ; Ante Bilušić ;
Mayank Jain ; Pavao Andričević

J. Appl. Phys. 139, 095104 (2026)
https://doi.org/10.1063/5.0314852

AIP Publishing

Journal of
Applied Physics

ARTICLE

pubs.aip.org/aip/jap

Optical and electrical signatures of charge trapping in hybrid perovskite $MAPbBr_3$ single crystals

Cite as: J. Appl. Phys. **139**, 095104 (2026); doi: 10.1063/5.0314852
Submitted: 2 December 2025 · Accepted: 9 February 2026 ·
Published Online: 3 March 2026

View Online Export Citation CrossMark

Frida Marie Lund Jeppesen,[1] Josipa Šćurla,[2,3] Milica Vasiljević,[4] Endre Horváth,[5,6] Ante Bilušić,[2] Mayank Jain,[1] and Pavao Andričević[1,7,a)]

AFFILIATIONS

[1] Department of Physics, Technical University of Denmark, DTU Risø Campus, Roskilde 4000, Denmark
[2] Faculty of Science, University of Split, Ruđera Boškovića 33, Split 21000, Croatia
[3] Faculty of Science, Doctoral Study of Biophysics, University of Split, Split, Croatia
[4] Department of Energy Conversion and Storage, Technical University of Denmark, Fysikvej, Building 310, Kgs. Lyngby 2800, Denmark
[5] Laboratory of Physics of Complex Matter, Ecole Polytechnique Fédérale de Lausanne, Lausanne 1015, Switzerland
[6] Institute for Medical Engineering and Medical Informatics, School of Life Sciences FHNW, Hofackerstrasse 30, 4132, Muttenz, Switzerland
[7] Dansk Fundamental Metrologi A/S, Hørsholm 2970, Denmark

[a)] **Author to whom correspondence should be addressed:** pra@dfm.dk

ABSTRACT

Understanding the dynamics of charge trapping and detrapping is essential for improving the optoelectronic performance of hybrid perovskite materials. In this study, we investigate temperature-dependent luminescence and electrical transport in single crystals of methylammonium lead bromide ($MAPbBr_3$). Radioluminescence and photoluminescence spectra collected from 8 to 300 K reveal multiple emission features, with several trap-related peaks disappearing at specific temperatures. These changes correlate with thermoluminescence measurements, which identify two prominent glow peaks corresponding to trap levels with activation energies of 69 and 126 meV, suggesting thermally driven release of carriers. Complementary current–voltage measurements performed at cryogenic temperatures exhibit clear trap-filled-limit and space-charge-limited current regimes, emerging only above 100 K. The absence of trap-filled-limit behavior at lower temperatures supports the presence of traps that hinder charge transport, consistent with the observed luminescence dynamics. Together, these results provide a coherent picture of thermal detrapping and carrier recombination in $MAPbBr_3$, offering insights relevant to perovskite-based optoelectronic applications.

INTRODUCTION

Organic–inorganic metal halide perovskites, commonly referred to as hybrid perovskites, are emerging as the next generation of semiconducting materials. With their extraordinary optoelectronic properties, this family of materials offers a wide range of applications, most notably in photovoltaics,[1,2] as well as in sensitive photodetection,[3,4] light emission,[5] gas sensing,[6] thermoelectrics,[7] piezoelectricity,[8] optically switched magnetism,[9,10] and exceptional radiation detection.[11–15]

Compared to other common semiconducting materials, hybrid perovskites possess a high density of intrinsic defects due to their soft, ionic lattices.[16,17] These defects can arise during crystallization or as a result of external factors.[18] Many of these defects act as trap sites where charge carriers can become localized, leading to non-radiative recombination, which often reduces the material's performance. Such trapping can result in lower open-circuit voltages, ultimately diminishing the efficiency of solar cells.[17] Additionally, it can decrease the photoluminescence (PL) quantum yield by providing non-radiative decay pathways, which lowers brightness and hinders the application of perovskites in light-emitting devices and scintillators.[19–23] Furthermore, traps can accelerate ion migration, which may lead either to material degradation and instability[24–26] or, under certain conditions, to defect self-healing.[14,27] Therefore, it is crucial to closely monitor both the nature of these defects and their associated trapping states, particularly their evolution under different operational conditions.

Various techniques are currently employed to track defects in perovskite materials. Structural properties are typically identified via electron paramagnetic resonance (EPR),[11] x-ray diffraction (XRD),[28,29] and transmission electron microscopy (TEM).[30] Regarding carrier dynamics. Photoconductivity (PC)[31,32] and photoconductance decay techniques (such as microwave-PCD[33,34] and time-resolved PC[35]) are of central importance for probing charge transport and trapping processes. Additionally, Raman spectroscopy and luminescence are widely used for examining optical properties and charge dynamics.[36–40]

This work will focus on luminescence. In semiconducting materials such as hybrid perovskites, luminescence serves as a powerful tool that provides insights into electronic structures and recombination processes, while also highlighting the influence of traps on charge carriers. Defects and their associated trap states create alternative recombination pathways, thereby directly affecting the luminescence properties of the material. By measuring the energy (or wavelength) of the emitted light, one can infer the presence of specific defects. Furthermore, studying luminescence as a function of temperature can yield valuable information about the nature of the defects.

In this study, we conducted photoluminescence (PL), radioluminescence (RL), and thermoluminescence (TL) measurements on methylammonium lead bromide (MAPbBr$_3$) single crystals (SCs). While fully inorganic perovskites (e.g., CsPbBr$_3$)[41] generally offer higher intrinsic thermal and chemical stability, hybrid systems remain favored for many optoelectronic applications due to their superior bandgap tunability and excellent charge-carrier transport. Within the hybrid family, MAPbBr$_3$, especially in its single crystalline form, has been shown to be significantly more stable compared to other hybrid perovskites commonly used in solar cells and light-emitting devices.[14,42,43] This makes it particularly interesting for radiation detection,[14] serving both as a direct detector and indirectly due to its ability to function as a scintillator that converts high-energy photons into visible light.[19,22] From the acquired spectra, we identified peaks that represent the radiative defect mediated recombination. By analyzing the temperature dependence of the spectra, we estimated the individual state energies. Finally, we performed current–voltage (I–V) measurements at cryogenic temperatures, allowing us to analyze the trap-filled-limit (TFL) behavior and extract trap densities,[44] which will further enhance our luminescence-based understanding of trap dynamics. This analysis will provide us with further insights into the trapping and detrapping mechanisms and their influence on various optoelectronic applications of this material.[45]

MATERIALS AND METHODS

Sample preparation

The MAPbBr$_3$ single crystals (SCs) used in this work were grown by the inverse temperature crystallization method.[14,44] To investigate the trapping mechanism, SCs of $1 \times 1 \times 0.5\ \mathrm{cm}^3$ were mounted in a custom made cryogenic luminescence setup at Risø Campus of DTU (Fig. 1).[46] The sample was attached by carbon paste to a cold finger, allowing us to vary its temperature from 8 K to room temperature.

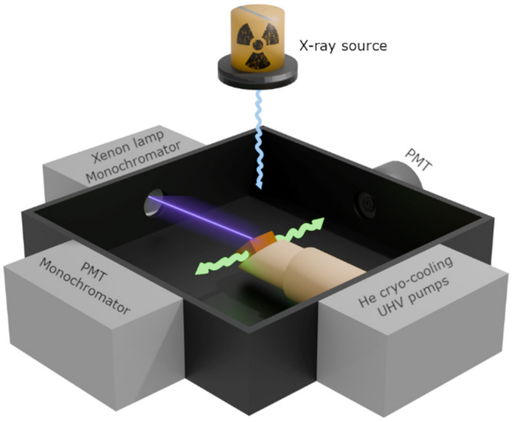

FIG. 1. Schematic of the luminescence measurements setup. The sample is positioned in the center of the setup, on a cold finger, at a 45° angle relative to both the xenon lamp in front and the x-ray source above the sample, facilitating PL and RL measurements. PMTs are positioned laterally to the described configuration, collecting the emitted light. The sample is cooled via He cryo-cooling and using ultrahigh vacuum (UHV) pumps connected to the cold finger.

Photoluminescence (PL) measurements

A xenon lamp (white light) paired with a double-grating monochromator (1200 lines/mm) is utilized to excite the sample at 400 nm for the PL measurements. The emitted light is subsequently collected by a Horiba iHR320 spectrograph (1200 lines/mm grating) and detected using a photomultiplier tube (PMT). To optimize the signal-to-noise ratio across the temperature range, slit widths were adjusted between 0.2 and 1.0 mm, resulting in an effective spectral resolution between 0.5 and 2.4 nm. This setup allows us to obtain a complete emission spectrum of our sample at a specific temperature.

Radioluminescence (RL) measurements

For the RL measurements, the light source was replaced with an x-ray source, specifically a palladium source emitting 46 keV x-ray photons. The emitted light is captured in the same manner as the PL by the spectrofluorometer.

Thermoluminescence (TL) measurements

In this experiment, a different PMT was used to detect the emitted light. This PMT measures total photon counts without providing spectral resolution. However, its enhanced sensitivity enables the reliable detection of low-intensity TL signals. The sample was initially cooled to 8 K. While at this temperature, it was irradiated with x rays for ≈30 min, during which the emitted light was simultaneously measured. After the x-ray source was turned off, the counts stabilized, establishing a background. The temperature was then increased to room temperature at a rate of 0.165 K/s while the TL signal was measured. All luminescence measurements were done at the Department of Physics, DTU Risø campus.

Data processing (Jacobian correction)

Since the luminescence spectra were initially recorded as photon counts per unit wavelength, they were converted to photon counts per unit energy using the Jacobian correction factor,[47] hc/E^2, to ensure correct representation of spectral intensities on an energy scale. All spectra presented in this work are shown after this correction.

Current–voltage (I–V) measurements

A $MAPbBr_3$ single crystal was measured in the dark using a two-contact configuration. Gold electrodes (25 μm thick) were thermally evaporated onto the opposing lateral faces of the crystal, and 25 μm diameter gold wires were attached using two-component silver epoxy (EPO-TEK EJ 2312). The crystal had approximate dimensions of 1.2 ± 0.1 mm in contact spacing and a cross-sectional area of 0.9 mm^2. Measurements were performed using a Keysight B2901A source-measure unit (SMU), operating in the voltage source and current measurement mode, with a theoretical current resolution down to 100 fA. A total of 2000 points were acquired per sweep, covering a voltage range from −42 to +42 V (limited by the instrument). The SMU was configured with a source delay of 10 ms, a measure delay of 10 ms, long integration time, and filtering enabled (time constant: 5 ms). Due to the high sample resistance (typically 100 MΩ–1 GΩ), four-point measurements were deemed unnecessary; however, special care was taken to minimize grounding and cable resistance effects (∼45 Ω per lead).

Trap density estimation

The trap density (N_t) was determined from the trap-filled-limit (TFL) voltage (V_{TFL}) obtained from the I–V characteristics, using the standard expression derived from the space-charge-limited current (SCLC) model, as follows:

$$N_t = \frac{2\varepsilon_r \varepsilon_0 V_{TFL}}{qL^2}, \tag{1}$$

where ε_r is the relative permittivity of the material, ε_0 is the vacuum permittivity, q is the elementary charge, and L is the distance between the electrodes. In this work, the parameters used were $\epsilon_r = 25$, $\epsilon_0 = 8.854 \times 10^{-12}\,\mathrm{F\,m^{-1}}$, $q = 1.602 \times 10^{-19}\,\mathrm{C}$, and $L = 1.2 \times 10^{-3}\,\mathrm{m}$. The trap-filled-limit voltage V_{TFL} was extracted from the kink point separating the trap-limited and trap-free regions in the log–log I–V curves.

RESULTS AND DISCUSSION

The $MAPbBr_3$ single crystals exhibit a sharp absorption edge at approximately 540 nm (≈2.3 eV). This confirms that using 400 nm excitation for PL measurements effectively generates carriers within the high-absorption region well above the bandgap.[44] The luminescence light yield is observed to be strongly temperature dependent. In Fig. 2, the total intensity for both PL and RL is plotted, revealing that it decays exponentially at equal rates as the temperature increases. This behavior is well-documented in semiconductors and scintillators and is referred to as the thermal quenching of luminescence.[48–50] As the temperature rises, nonradiative recombination pathways become increasingly active. For instance, electrons or holes that would typically recombine radiatively (emitting light) are instead captured by trap states or phonons, which dissipate the energy as heat. Specifically, above 100–150 K, these alternative recombination pathways begin to dominate. Additionally, the phase transition of $MAPbBr_3$ from orthorhombic to tetragonal at approximately 150 K may significantly influence defect and trap reconfiguration,[51] thereby affecting the luminescence data.

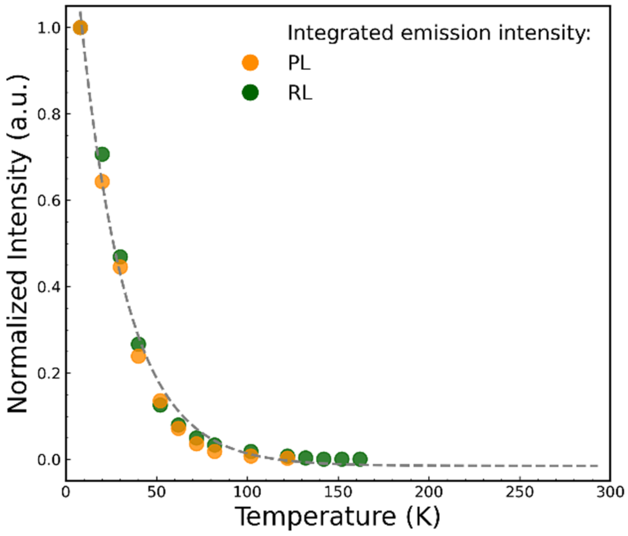

FIG. 2. Normalized PL and RL intensities of $MAPbBr_3$ single crystals follow the same exponential decay trend (dashed curve) with temperature. Both intensities saturate at zero around 150 K.

To better understand the defect dynamics and recombination mechanisms, the focus was turned to analyzing the spectral shape of the emission. Both PL and RL spectra were collected in the temperature range from 8 to 300 K (Fig. 3). Compared to PL, the RL spectra reveal additional emission peaks. This difference arises from the bulk-sensitive excitation of RL, allowing the detection of defect states located deeper inside the crystal that are either not excited by surface-limited PL or whose emission is spectrally blended and, thus, unresolved in PL spectra.[19,52] In PL spectra, overlapping broad features can obscure individual transitions, masking distinct defect-related emissions. Consequently, RL spectra were primarily used in this work for peak identification and energetic analysis as they provide higher resolution and clearer separation of emission bands. It should be noted that the lateral collection geometry may induce a slight redshift and high-energy attenuation due to self-absorption, an effect more pronounced in surface-limited PL than in volumetric RL. A 2D map of normalized PL and RL spectra as a function of temperature and emission energy is provided in Fig. S1 in the supplementary material, complementing the stacked spectra in Fig. 3.

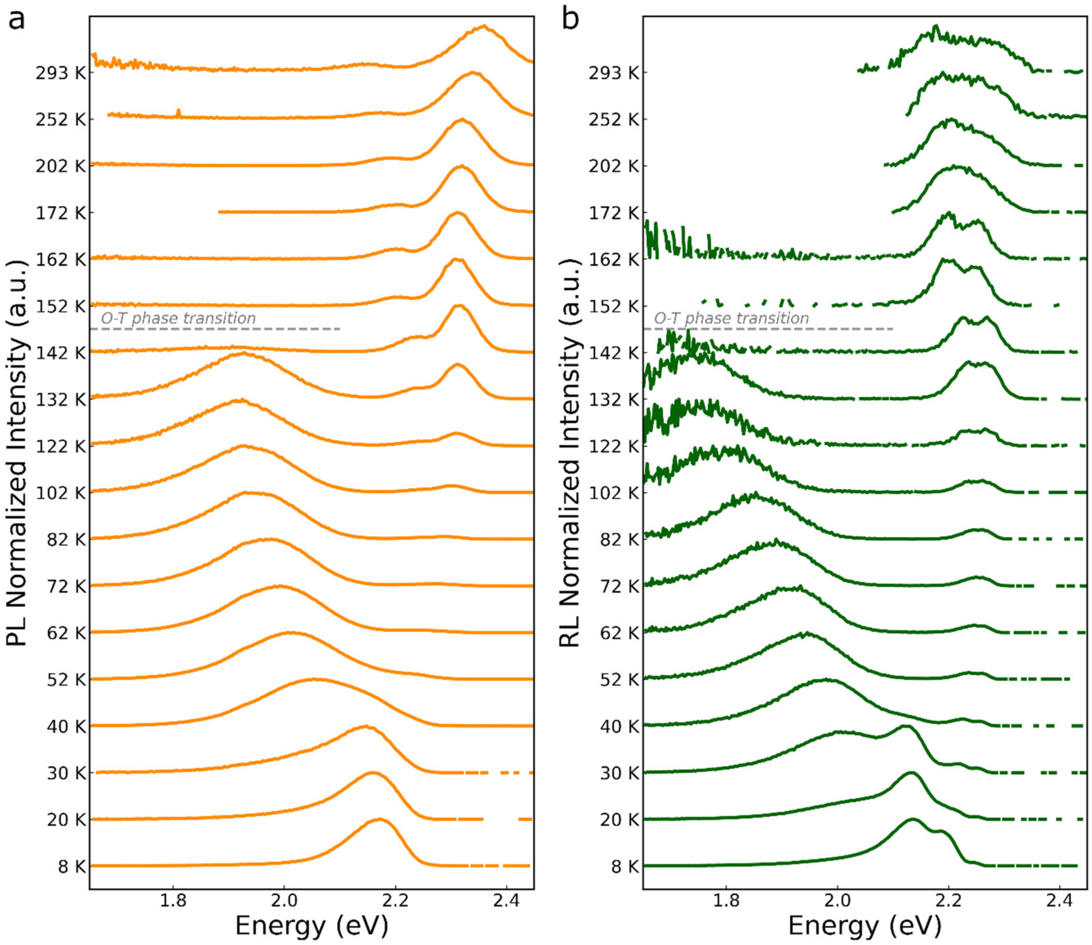

FIG. 3. Temperature-dependent (a) PL and (b) RL spectra of $MAPbBr_3$ single crystals measured from 8 to 300 K in different temperature steps at 400 nm and 46 keV photons, respectively. The orthorhombic-to-tetragonal (O–T) phase transition temperature is depicted by the grey dashed line.

At low temperatures (8–50 K), the contours of multiple individual peaks are observed in the RL spectra [Fig. 3(b)]. Two peaks are located around 2.25 eV, corresponding to the bandgap energy of $MAPbBr_3$. The fraction of total photon emission detected from these peaks starts off small but increases with temperature, remaining consistently observable up to room temperature. The third peak, cantered at 2.14 eV, is clearly detectable below 50 K. This peak may originate from recombination at a defect center fed by a shallow trap state that begins to empty due to thermal detrapping at approximately 50 K. An additional sub-bandgap peak, centered at around 2.0 eV, emerges at 8 K. The fraction of total counts from this 2.0 eV emission initially increases as the 2.14 eV peak fades, suggesting a redistribution of carriers toward these deeper centers once the shallowest trap is exhausted. This 2.0 eV feature remains prominent until approximately 80 K, eventually disappearing by 150 K.[53] This disappearance coincides with the known orthorhombic-to-tetragonal phase transition in $MAPbBr_3$. Furthermore, a steady redshift of this broad lower-energy peak is observed as the temperature increases. This peak may originate from radiative defect states, either shallow or moderately deep, associated with a recombination center that redshifts with rising temperature. This shift is consistent with carriers thermally relaxing into the lower-energy tail of the defect density of states at higher temperatures. Its absence above 150 K supports the assignment to localized defect states whose radiative recombination is quenched by non-radiative processes, thermally detrapped, or structurally suppressed in the higher-symmetry phase.

The RL spectra were fitted to a sum of Gaussian functions (Fig. S2 in the supplementary material). At temperatures below 50 K, the best fit is achieved by summing five Gaussians, suggesting that the broad peak observed at lower energies (<2 eV) may be composed of two individual peaks. Above 50 K, a satisfactory fit can be obtained with a sum of four Gaussians, while at temperatures exceeding 150 K, only the two peaks near the bandgap energy remain. Figure 4(a) illustrates the fit of the RL spectrum at 30 K as an example. It is assumed that the energetic order of the peak centers is preserved throughout the temperature range. The central

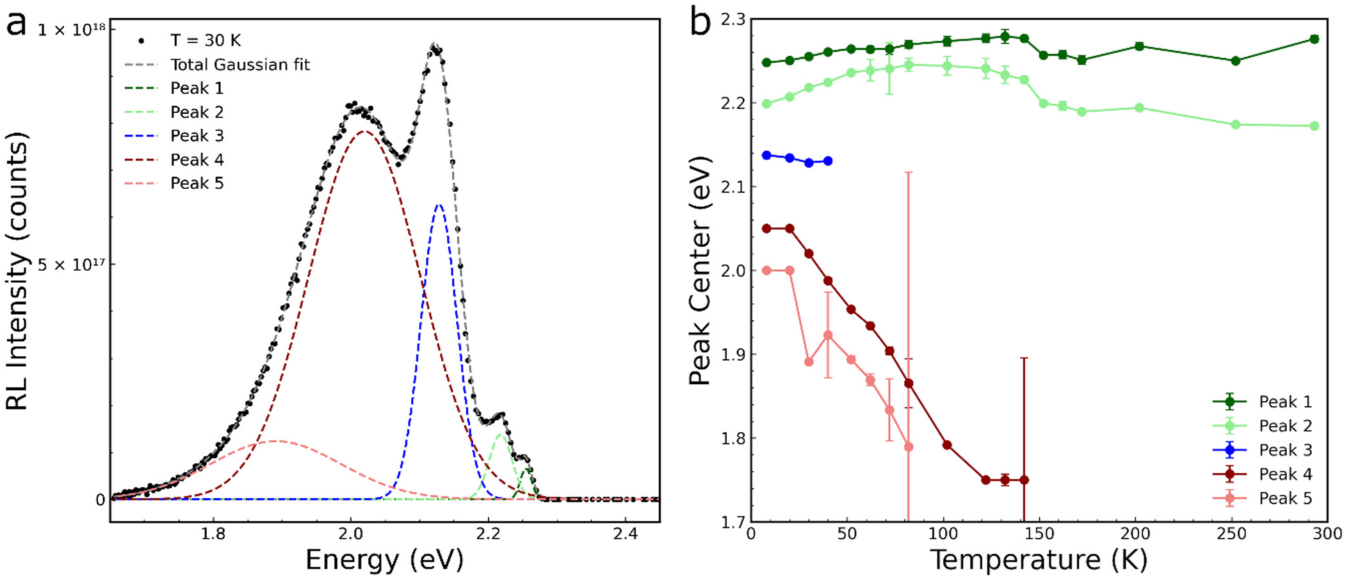

FIG. 4. (a) RL spectrum at 30 K fitted with five Gaussian components representing distinct emission features. (b) Temperature evolution of the fitted peak positions extracted from multi-Gaussian fits at each temperature, showing the thermal shifts of individual emission centers.

positions of the peaks, determined through fitting, are plotted vs temperature in Fig. 4(b). The center emission energies of peaks 4 and 5 decrease approximately linearly, from 2.09 to 1.70 eV and from 1.95 to 1.58 eV, respectively. The center emission energy of peak 3 remains constant at 2.14 eV in measurements from 8 to 50 K, while this peak cannot be distinguished at higher temperatures. The emission energies of peaks 1 and 2 initially show a slight increase as the temperature rises, followed by a small drop around 150 K, coinciding with the phase transition temperature.[53] From 152 to 293 K, the centers of these two peaks diverge, reaching a separation of 100 meV at room temperature (2.18 and 2.28 eV). Higher-energy peak 1 is attributed to free exciton recombination near the band edge, while lower-energy peak 2 likely arises from bound excitons or shallow defect-assisted radiative processes and remains visible up to room temperature due to its greater thermal stability. The transition from the tetragonal to the cubic phase occurs at 236.9 K and does not seem to affect the RL nor the PL spectra significantly.[53] Corresponding temperature dependence of peak widths and intensities is presented in Fig. S3 in the supplementary material.

The disappearance of peaks with increasing temperature suggests thermally activated detrapping; consequently, TL measurements were performed. After irradiating the single crystal with x rays at 8 K for ≈30 min (Fig. S4 in the supplementary material), the sample was steadily heated up to room temperature. As shown in Fig. 5, following a decaying signal attributed to residual luminescence/afterglow at 8 K, two distinct emissions of light were detected at approximately 50 and 100 K. These emissions indicate that at least some of the sub-bandgap, emission peaks originate from recombination occurring via shallow defect states, with corresponding detrapping activation energies on the order of a few tens to a hundred meV. The TL data were fitted to the approximate expression for the TL intensity of first-order TL glow curves, as derived by Kitis *et al.*[54] The assignment of first-order kinetics is supported by the observed stability of the peak temperature across different irradiation doses (Fig. S5 in the supplementary material). The combined fit for both peaks is plotted as the gray curve in Fig. 5. Table I shows the fitted parameters: peak temperature T_{max}, peak intensity I_{max}, and activation energy E_a.

The thermal decay of RL emission peak 3 (≈2.14 eV) is strongly correlated with the TL glow peak observed near 50 K. This TL peak arises from the thermal release of carriers from a shallow trap state with a calculated activation energy of 69 meV. It is important to note that E_a represents the thermal barrier that carriers must overcome to escape the trap, while the 2.14 eV emission energy is released during the subsequent radiative recombination at the luminescence center. The observation that the RL signal vanishes near 50 K (Fig. S3b in the supplementary material) confirms that the thermal emptying of this trap is the primary source feeding the luminescence center, with its emptying leading directly to the disappearance of the emission. Notably, the close agreement between the disappearance of the steady-state RL signal and the occurrence of the dynamic TL peak at 50 K provides internal validation of our temperature calibration. Despite the relatively large crystal dimensions and the ultra-low thermal conductivity characteristic of hybrid perovskites (0.44–0.5 W/m K),[55] the alignment of these features suggests that thermal lag between the crystal surface and the sensor was minimal (≈5 K).

The second TL glow peak, cantered at 97 K, is strongly correlated with the thermal quenching of RL emission peak 5 (which shifts from ≈2.0 to 1.8 eV). This peak arises from the thermal release of carriers from a relatively deeper trap state, with a

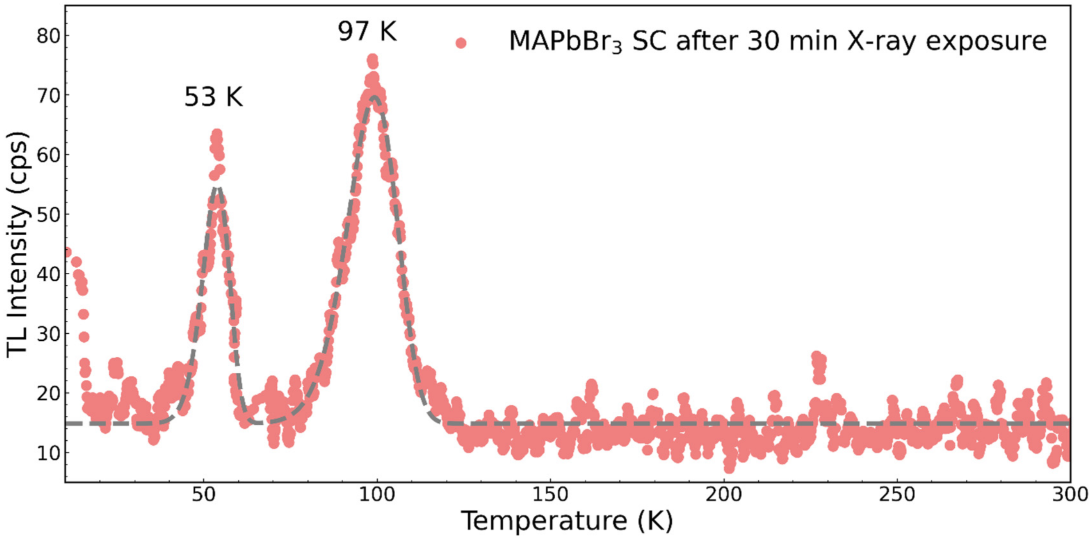

FIG. 5. TL signal of the $MAPbBr_3$ single crystal measured from 8 to 300 K (red dots) and the appropriate TL glow curve fits (gray dashed line).

calculated activation energy of 126.6 meV. The observation that RL peak 5 begins its rapid decay around 70 K, coincident with the emergence of the TL peak, and disappears completely near 100 K (Fig. S3b in the supplementary material) confirms that the thermal emptying of this trap is the primary mechanism responsible for quenching this specific luminescence band. As previously mentioned, peak 4 from the RL emission, which disappears after 150 K, is attributed to a structural phase transition and does not produce a corresponding TL glow peak. The absence of a TL signal confirms that the disappearance of peak 4 results from a thermodynamic change in the perovskite crystal structure, not the thermal release and recombination of trapped charge carriers. While current data strongly point to a structural origin, further studies using temperature-dependent Time-resolved PL (TRPL) or EPR across the transition could help to unambiguously distinguish between a purely structural reconfiguration and a complex thermal quenching process.

Current–voltage (I–V) characteristics were measured at four different cryogenic temperatures: 50, 100, 150, and 200 K. To distinguish between different transport regimes and to extract the voltage dependence of the current, the I–V curves are plotted on a double logarithmic scale, where linear regions correspond to power-law behavior $I \propto V^n$. At 50 and 100 K [Fig. 6(a)], the I–V characteristics exhibit sub-ohmic behavior ($n < 1$),[56] with current scaling reaching a maximum of 0.6. The sub-linear dependence suggests that charge transport in the crystal is limited not only by the Schottky barrier at the metal–semiconductor interfaces but, more importantly, by trap states that capture injected carriers and impede their motion.[57] These traps introduce energetic barriers for carrier transport, particularly at low temperatures, where their effect becomes even more pronounced.

TABLE I. Parameters of the first-order TL glow curve fits to the TL spectrum of the $MAPbBr_3$ single crystal.

T_{max}(K)	I_{max}(counts/s)	E_a(meV)
52.7 ± 0.1	38.3 ± 0.7	69.0 ± 1.3
97.0 ± 0.1	52.3 ± 0.5	126.6 ± 1.4

This low-conduction behavior correlates with our luminescence data. Below 100 K, the PL and RL spectra exhibit strong emission intensity and multiple distinct peaks (3, 4, and 5), indicating a high density of radiative recombination centers associated with localized defect states. The simultaneous presence of strong light emission and suppressed electrical conduction reflects a scenario in which photo-generated carriers are rapidly trapped and recombine radiatively before contributing to current transport.

On the other hand, at temperatures of 150 and 200 K [Fig. 6(b)], the I–V characteristics evolve significantly, revealing all three distinct regimes typical of trap-limited space-charge-limited current (SCLC) transport.[44] The low-voltage region continues to exhibit sub-ohmic behavior ($n = 0.69$ and $n = 0.38$); however, a pronounced transition to a trap-filled-limit (TFL) regime occurs at approximately 1.5 and 2.5 V, respectively. At this point, the current sharply increases, with slopes of $n = 7.36$ and $n = 5.81$. This marks the saturation of available trap states with injected carriers. At higher voltages (>6 V), the slope decreases again to values slightly above $n = 2$, consistent with the trap-free SCLC regime described by the Mott–Gurney law, where the current is governed by the space-charge of free carriers. For 150 K, a deviation from linearity is observed above approximately 15 V, likely arising from non-ideal effects such as ion migration or sample heating.

The emergence of a well-defined TFL regime at higher temperatures indicates a simplification of the trap landscape. At these temperatures, shallow trap states, responsible for the complex transport behavior observed at lower temperatures, become thermally

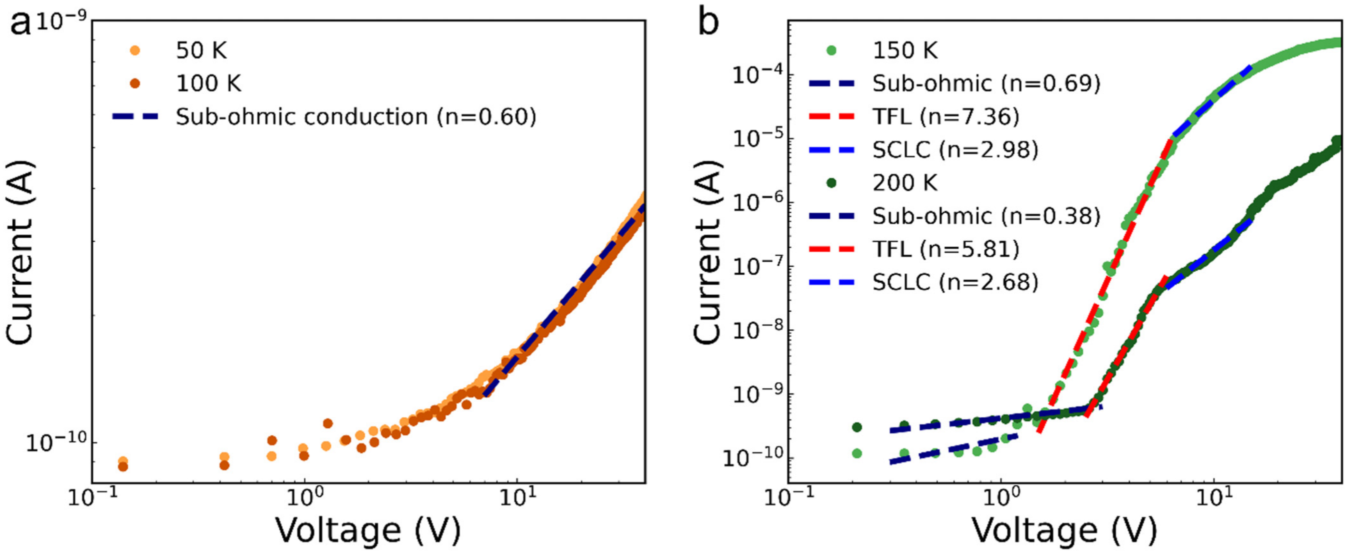

FIG. 6. Current–voltage (I–V) characteristics of $MAPbBr_3$ single crystals measured at (a) 50, 100, (b) 150, and 200 K. The curves are plotted on a double logarithmic scale to identify transport regimes, with linear fits indicating the voltage scaling exponent n in different regions: sub-ohmic ($n < 1$), trap-filled limit ($n > 2$), and space-charge-limited current ($n \approx 2$).

inactive because the rate of thermal release significantly exceeds the capture rate. Consequently, the injected carriers primarily interact with the remaining deeper trap states. The sharp increase in current observed in Fig. 6(b), thus, corresponds to the saturation of these stable deep traps. This transition enables more efficient carrier injection, as transport is no longer impeded by the variety of shallow states active at cryogenic temperatures. These trends are reflected in the luminescence data. Below 100 K, TL glow peaks reveal the thermal release of carriers from shallow traps, confirming that these states gradually empty as the temperature increases. Above 100 K, both PL and RL intensities decrease markedly, and the number of spectral peaks is reduced, implying a lower density of active radiative centers. The convergence of these optical and electrical observations, thus, highlights a clear transition in trap dynamics between 100 and 150 K, where the trap landscape shifts from a complex, multi-level trapping regime to one dominated by the filling of specific deep-level defects.

Using the trap-filled-limit voltage V_{TFL} extracted from the I–V curves, we estimated the trap density N_t. The calculated values lie in the range of approximately 2.9×10^9–$5.8 \times 10^9\,\mathrm{cm^{-3}}$, consistent with moderate trap concentrations typically observed in high-quality hybrid perovskite single crystals.[44] Notably, these values are several orders of magnitude lower than those found in polycrystalline perovskite thin films (10^{15}–$10^{17}\,\mathrm{cm^{-3}}$) (Ref. 1) or conventional thin-film semiconductors like CdTe (10^{13}–$10^{15}\,\mathrm{cm^{-3}}$),[58] and they approach the exceptional purity levels of electronic-grade monocrystalline silicon.[59] The absence of a distinct TFL region below 100 K suggests a higher trap density, likely exceeding $10^{10}\,\mathrm{cm^{-3}}$.[60] This finding, once again, aligns with our optical measurements, which demonstrate enhanced luminescence and multiple defect-related emission peaks at these lower temperatures.

While these I–V characteristics were recorded in the dark, under visible light or x-ray illumination, photogenerated carriers would pre-fill the shallow traps identified via TL (69 and 126 meV), likely converting the low-temperature sub-ohmic behavior into a more efficient ohmic transport regime. At higher temperatures, the pre-filling would reduce the V_{TFL} or saturate the traps entirely, potentially allowing a direct transition into the trap-free SCLC regime. This shift represents a transition to a transport regime governed primarily by the density of radiation-generated free carriers.

CONCLUSION

This study presents a comprehensive analysis of trap states in $MAPbBr_3$ single crystals by combining PL, RL, TL, and I–V measurements over a broad temperature range. Five distinct RL peaks were identified: one observable only below 50 K, and two that disappear between 100 and 150 K, both exhibiting a redshift with increasing temperature. Two additional RL peaks persist up to room temperature and closely correspond to the band gap energy, showing only minor shifts around the structural phase transition at approximately 150 K. TL measurements revealed two prominent trap levels with activation energies of about 69 and 126 meV, which correlate well with the temperature-dependent quenching of specific RL peaks. The specific atomic nature of these traps is not yet fully defined; previous studies suggest that they could be bromine vacancy centres,[61] but further investigations are needed to confirm their origin.

Electrical characterization further corroborated the optical findings. At low temperatures (50 K and 100 K), I–V curves display sub-ohmic conduction, indicative of severe limitations in charge injection and transport. While TL measurements confirm the presence of shallow traps, their behavior at cryogenic temperatures resembles that of deep traps, effectively immobilizing carriers and suppressing conduction. Above 100 K (150 and 200 K), distinct trap-filled-limit (TFL) and space-charge-limited current (SCLC) regimes emerge, suggesting that traps become increasingly filled or inactive as the temperature rises, coinciding with a reduction in luminescence due to both thermal detrapping and quenching. Trap densities estimated from the I–V data are on the order of 10^9 cm^{-3} at higher temperatures, while deeper traps below 100 K likely exceed 10^{10} cm^{-3}.

These findings have important implications for potential device applications. At room temperature, the absence of pronounced defect-related luminescence features in RL and the relatively low trap density inferred from I–V measurements (on the order of 10^9 cm^{-3}) suggest that trap-assisted recombination is minimal, which is favorable for optoelectronic devices such as LEDs, solar cells, and detectors operating at room temperature. However, the emergence of multiple defect-related emission peaks in RL at low temperatures, along with the disappearance of the TFL regime in I–V measurements below 100 K, indicates a significant increase in trap effects under cryogenic conditions. Although many of these traps are energetically shallow, they effectively behave as deep traps in this temperature range because the thermal energy is insufficient for efficient detrapping. This implies that devices designed to operate at cryogenic temperatures, such as x-ray detectors, space photovoltaics, or quantum light sources, may experience reduced carrier mobility, decreased light yield, increased afterglow, or broadened timing response. These results underscore the need for targeted defect passivation strategies, especially for low-temperature applications, even when room-temperature performance appears unaffected.

SUPPLEMENTARY MATERIAL

Detailed 2D normalized PL and RL maps (Fig. S1); Gaussian deconvolution of RL spectra (Fig. S2) and extracted peak parameters [full width at half maximum (FWHM) and intensity] across 8–300 K (Fig. S3); stability of the RL signal during x-ray pre-irradiation (Fig. S4); and TL dose-dependence measurements (Fig. S5) are provided in the supplemental material.

ACKNOWLEDGMENTS

This work was supported by funds from the Danish Agency for Higher Education and Science.

AUTHOR DECLARATIONS

Conflict of Interest

The authors have no conflicts to disclose.

Author Contributions

Frida Marie Lund Jeppesen: Investigation (equal); Writing – review & editing (equal). **Josipa Šćurla:** Investigation (equal); Writing – review & editing (equal). **Milica Vasiljević:** Formal analysis (supporting); Writing – review & editing (supporting). **Endre Horváth:** Resources (equal). **Ante Bilušić:** Methodology (equal); Supervision (equal). **Mayank Jain:** Methodology (equal); Supervision (equal). **Pavao Andričević:** Conceptualization (lead); Formal analysis (lead); Project administration (lead); Resources (equal); Supervision (lead); Writing – original draft (lead).

DATA AVAILABILITY

The data that support the findings of this study are available from the corresponding author upon reasonable request.

REFERENCES

[1] M. A. Green, A. Ho-Baillie, and H. J. Snaith, "The emergence of perovskite solar cells," Nat. Photonics **8**(7), 506–514 (2014).

[2] J. Huang, Y. Yuan, Y. Shao, and Y. Yan, "Understanding the physical properties of hybrid perovskites for photovoltaic applications," Nat. Rev. Mater. **2**, 17042 (2017).

[3] P. Andričević, M. Kollár, X. Mettan, B. Náfrádi, A. Sienkiewicz, D. Fejes, K. Hernádi, L. Forró, and E. Horváth, "Three-dimensionally enlarged photoelectrodes by a protogenetic inclusion of vertically aligned carbon nanotubes into $CH_3NH_3PbBr_3$ single crystals," J. Phys. Chem. C **121**(25), 13549–13556 (2017).

[4] Z. K. Tan, R. S. Moghaddam, M. L. Lai, P. Docampo, R. Higler, F. Deschler, M. Price, A. Sadhanala, L. M. Pazos, D. Credgington, F. Hanusch, T. Bein, H. J. Snaith, and R. H. Friend, "Bright light-emitting diodes based on organometal halide perovskite," Nat. Nanotechnol. **9**(9), 687–692 (2014).

[5] P. Andričević, X. Mettan, M. Kollár, B. Náfrádi, A. Sienkiewicz, T. Garma, L. Rossi, L. Forró, and E. Horváth, "Light-emitting electrochemical cells of single crystal hybrid halide perovskite with vertically aligned carbon nanotubes contacts," ACS Photonics **6**(4), 967–975 (2019).

[6] K. Mantulnikovs, A. Glushkova, P. Matus, L. Ćirić, M. Kollár, L. Forró, E. Horváth, and A. Sienkiewicz, "Morphology and photoluminescence of CH_3 NH_3 PbI_3 deposits on nonplanar, strongly curved substrates," ACS Photonics **5**(4), 1476–1485 (2018).

[7] X. Mettan, R. Pisoni, P. Matus, A. Pisoni, J. Jacimovic, B. Náfrádi, M. Spina, D. Pavuna, L. Forró, and E. Horváth, "Tuning of the thermoelectric figure of merit of CH_3 NH_3 MI_3 ($M = Pb,Sn$) photovoltaic perovskites," J. Phys. Chem. C **119**(21), 11506 (2015).

[8] M. Vasiljevic, M. Kollár, D. Spirito, L. Riemer, L. Forró, E. Horváth, S. Gorfman, and D. Damjanovic, "'Forbidden' polarisation and extraordinary piezoelectric effect in organometallic lead halide perovskites," Adv. Funct. Mater. **32**(40), 2204898 (2022).

[9] B. Náfrádi, P. Szirmai, M. Spina, H. Lee, O. V. Yazyev, A. Arakcheeva, D. Chernyshov, M. Gibert, L. Forró, and E. Horváth, "Optically switched magnetism in photovoltaic perovskite $CH_3NH_3(Mn{:}Pb)I_3$," Nat. Commun. **7**, 13406 (2016).

[10] M. Wang, H. Xu, T. Wu, H. Ambaye, J. Qin, J. Keum, I. N. Ivanov, V. Lauter, and B. Hu, "Optically induced static magnetization in metal halide perovskite for spin-related optoelectronics," Adv. Sci. **8**(11), 2004488 (2021).

[11] P. Andricevic, P. Frajtag, P. Szirmai, G. Náfrádi, M. Kollár, L. Forró, E. Horváth, and A. Pautz, "Perovskite-based detector for reactor dosimetry monitoring," in *EPJ Web Conference* (EDP Sciences, 2024), Vol. 308, p. 01010.

[12] P. Andričević, G. Náfrádi, M. Kollár, B. Náfrádi, S. Lilley, C. Kinane, P. Frajtag, A. Sienkiewicz, A. Pautz, E. Horváth, and L. Forró, "Hybrid halide perovskite neutron detectors," Sci. Rep. **11**(1), 17159 (2021).

[13] A. Glushkova, P. Andričević, R. Smajda, B. Náfrádi, M. Kollár, V. Djokić, A. Arakcheeva, L. Forró, R. Pugin, and E. Horváth, "Ultrasensitive 3D aerosol-jet-printed perovskite x-ray photodetector," ACS Nano **15**(3), 4077–4084 (2021).

[14] P. Andričević, P. Frajtag, V. P. Lamirand, A. Pautz, M. Kollár, B. Náfrádi, A. Sienkiewicz, T. Garma, L. Forró, and E. Horváth, "Kilogram-scale crystallogenesis of halide perovskites for gamma-rays dose rate measurements," Adv. Sci. **8**(2), 2001882 (2021).

[15] L. Li, X. Liu, H. Zhang, B. Zhang, W. Jie, P. J. Sellin, C. Hu, G. Zeng, and Y. Xu, "Enhanced x-ray sensitivity of MAPbBr$_3$ detector by tailoring the interface-states density," ACS Appl. Mater. Interfaces **11**(7), 7522–7528 (2019).

[16] S. G. Motti, D. Meggiolaro, S. Martani, R. Sorrentino, A. J. Barker, F. De Angelis, and A. Petrozza, "Defect activity in lead halide perovskites," Adv. Mater. **31**(47), 1–11 (2019).

[17] H. Jin, E. Debroye, M. Keshavarz, I. G. Scheblykin, M. B. J. Roeffaers, and J. A. Steele, "It's a trap! on the nature of localised states and charge trapping in lead halide perovskites," Mater. Horiz. **7**(2), 397–410 (2020).

[18] C. Wang, Z. Xie, Y. Wang, Y. Ding, M. K. H. Leung, and Y. H. Ng, "Defects of metal halide perovskites in photocatalytic energy conversion: Friend or foe?," Adv. Sci. **11**(29), 2402471 (2024).

[19] M. D. Birowosuto, D. Cortecchia, W. Drozdowski, K. Brylew, W. Lachmanski, and A. Bruno, "X-ray scintillation in lead halide perovskite crystals," Sci. Rep. **6**(1), 37254 (2016).

[20] Y. Zhang, R. Sun, X. Ou, K. Fu, Q. Chen, Y. Ding, L. J. Xu, L. Liu, Y. Han, A. V. Malko, X. Liu, H. Yang, O. M. Bakr, H. Liu, and O. F. Mohammed, "Metal halide perovskite nanosheet for x-ray high-resolution scintillation imaging screens," ACS Nano **13**(2), 2520–2525 (2019).

[21] C. Rodà, M. Fasoli, M. L. Zaffalon, F. Cova, V. Pinchetti, J. Shamsi, A. L. Abdelhady, M. Imran, F. Meinardi, L. Manna, A. Vedda, and S. Brovelli, "Understanding thermal and a-thermal trapping processes in lead halide perovskites towards effective radiation detection schemes," Adv. Funct. Mater. **31**(43), 2104879 (2021).

[22] V. B. Mykhaylyk, H. Kraus, and M. Saliba, "Bright and fast scintillation of organolead perovskite MAPbBr$_3$ at low temperatures," Mater. Horiz. **6**(8), 1740–1747 (2019).

[23] S. Mahato, M. Makowski, S. Bose, D. Kowal, M. A. Kuddus Sheikh, P. Braueninger-Wemer, M. E. Witkowski, S. K. Ray, W. Drozdowski, and M. D. Birowosuto, "Improvement of light output of MAPbBr$_3$ single crystal for ultrafast and bright cryogenic scintillator," J. Phys. Chem. Lett. **15**(14), 3713–3720 (2024).

[24] S. Baumann, G. E. Eperon, A. Virtuani, Q. Jeangros, D. B. Kern, D. Barrit, J. Schall, W. Nie, G. Oreski, M. Khenkin, C. Ulbrich, R. Peibst, J. S. Stein, and M. Köntges, "Stability and reliability of perovskite containing solar cells and modules: Degradation mechanisms and mitigation strategies," Energy Environ. Sci. **17**(20), 7566–7599 (2024).

[25] D. Moia and J. Maier, "Ion transport, defect chemistry, and the device physics of hybrid perovskite solar cells," ACS Energy Lett. **6**(4), 1566–1576 (2021).

[26] A. Musiienko, D. R. Ceratti, J. Pipek, M. Brynza, H. Elhadidy, E. Belas, M. Betušiak, G. Delport, and P. Praus, "Defects in hybrid perovskites: The secret of efficient charge transport," Adv. Funct. Mater. **31**(48), 2104467 (2021).

[27] C. Wang, D. Qu, B. Zhou, C. Shang, X. Zhang, Y. Tu, and W. Huang, "Self-healing behavior of the metal halide perovskites and photovoltaics," Small **20**(6), 2307645 (2024).

[28] O. Er-Raji, L. Rustam, B. P. Kore, S. W. Glunz, and P. S. C. Schulze, "Insights into perovskite film formation using the hybrid evaporation/spin-coating route: An *in situ* XRD study," ACS Appl. Energy Mater. **6**(11), 6183–6193 (2023).

[29] K. H. Wang, L. C. Li, M. Shellaiah, and K. W. Sun, "Structural and photophysical properties of methylammonium lead tribromide (MAPbBr$_3$) single crystals," Sci. Rep. **7**(1), 13643 (2017).

[30] R. Sainju, W. Y. Chen, S. Schaefer, Q. Yang, C. Ding, M. Li, and Y. Zhu, "Defecttrack: A deep learning-based multi-object tracking algorithm for quantitative defect analysis of in-situ TEM videos in real-time," Sci. Rep. **12**(1), 15705 (2022).

[31] Y. Chen, H. T. Yi, X. Wu, R. Haroldson, Y. N. Gartstein, Y. I. Rodionov, K. S. Tikhonov, A. Zakhidov, X. Y. Zhu, and V. Podzorov, "Extended carrier lifetimes and diffusion in hybrid perovskites revealed by Hall effect and photoconductivity measurements," Nat. Commun. **7**, 12253 (2016).

[32] J. Lim, M. Kober-Czerny, Y. H. Lin, J. M. Ball, N. Sakai, E. A. Duijnstee, M. J. Hong, J. G. Labram, B. Wenger, and H. J. Snaith, "Long-range charge carrier mobility in metal halide perovskite thin-films and single crystals via transient photo-conductivity," Nat. Commun. **13**(1), 4201 (2022).

[33] A. Bojtor, S. Kollarics, B. G. Márkus, A. Sienkiewicz, M. Kollár, L. Forró, and F. Simon, "Ultralong charge carrier recombination time in methylammonium lead halide perovskites," ACS Photonics **9**(10), 3341–3350 (2022).

[34] A. Bojtor, D. Krisztián, F. Korsós, S. Kollarics, G. Paráda, T. Pinel, M. Kollár, E. Horváth, X. Mettan, H. Shiozawa, B. G. Márkus, L. Forró, and F. Simon, "Millisecond-scale charge-carrier recombination dynamics in the CsPbBr$_3$ perovskite," Adv. Energy Sustainability Res. **5**(9), 2400043 (2024).

[35] G. R. Yettapu, D. Talukdar, S. Sarkar, A. Swarnkar, A. Nag, P. Ghosh, and P. Mandal, "Terahertz conductivity within colloidal CsPbBr$_3$ perovskite nanocrystals: Remarkably high carrier mobilities and large diffusion lengths," Nano Lett. **16**(8), 4838–4848 (2016).

[36] Z. Zhang, J. Zhang, Z.-J. Liu, N. S. Dahod, W. Paritmongkol, N. Brown, A. Stollmann, W. S. Lee, Y.-C. Chien, Z. Dai, K. A. Nelson, W. A. Tisdale, A. M. Rappe, and E. Baldini, "Discovery of enhanced lattice dynamics in a single-layered hybrid perovskite," Sci. Adv. **9**(33), eadg4417 (2023).

[37] A. Merdasa, M. Bag, Y. Tian, E. Källman, A. Dobrovolsky, and I. G. Scheblykin, "Super-resolution luminescence microspectroscopy reveals the mechanism of photoinduced degradation in CH$_3$NH$_3$PbI$_3$ perovskite nanocrystals," J. Phys. Chem. C **120**(19), 10711–10719 (2016).

[38] B. J. Bohn, Y. Tong, M. Gramlich, M. L. Lai, M. Döblinger, K. Wang, R. L. Z. Hoye, P. Müller-Buschbaum, S. D. Stranks, A. S. Urban, L. Polavarapu, and J. Feldmann, "Boosting tunable blue luminescence of halide perovskite nanoplatelets through postsynthetic surface trap repair," Nano Lett. **18**(8), 5231–5238 (2018).

[39] V. I. Yudin, M. S. Lozhkin, A. V. Shurukhina, A. V. Emeline, and Y. V. Kapitonov, "Photoluminescence manipulation by ion beam irradiation in CsPbBr$_3$ halide perovskite single crystals," J. Phys. Chem. C **123**(34), 21130–21134 (2019).

[40] Y. Xu, X. Wang, S. Liu, Y. Pan, A. Perveen, D. C. Onwudiwe, O. E. Fayemi, E. E. Elemike, B. S. Bae, Y. Zhu, R. Z. Talaighil, X. Zhang, J. Chen, Z. Zhao, Q. Li, W. Lei, and X. Xu, "Sensitive thermography via sensing visible photons detected from the manipulation of the trap state in MAPbX$_3$," ACS Appl. Mater. Interfaces **15**(48), 56526–56536 (2023).

[41] S. Ullah, J. Wang, P. Yang, L. Liu, S. E. Yang, T. Xia, H. Guo, and Y. Chen, "All-inorganic CsPbBr$_3$ perovskite: A promising choice for photovoltaics," Mater. Adv. **2**(2), 646–683 (2021).

[42] A. G. Boldyreva, L. A. Frolova, I. S. Zhidkov, L. G. Gutsev, E. Z. Kurmaev, B. R. Ramachandran, V. G. Petrov, K. J. Stevenson, S. M. Aldoshin, and P. A. Troshin, "Unravelling the material composition effects on the gamma ray stability of lead halide perovskite solar cells: MAPbI$_3$ breaks the records," J. Phys. Chem. Lett. **11**(7), 2630–2636 (2020).

[43] B. Murali, H. K. Kolli, J. Yin, R. Ketavath, O. M. Bakr, and O. F. Mohammed, "Single crystals: The next big wave of perovskite optoelectronics," ACS Mater. Lett. **2**(2), 184–214 (2020).

[44] M. I. Saidaminov, A. L. Abdelhady, B. Murali, E. Alarousu, V. M. Burlakov, W. Peng, I. Dursun, L. Wang, Y. He, G. Maculan, A. Goriely, T. Wu, O. F. Mohammed, and O. M. Bakr, "High-quality bulk hybrid perovskite single crystals within minutes by inverse temperature crystallization," Nat. Commun. **6**(1), 7586 (2015).

[45] V. S. Chirvony, S. González-Carrero, I. Suárez, R. E. Galian, M. Sessolo, H. J. Bolink, J. P. Martínez-Pastor, and J. Pérez-Prieto, "Delayed luminescence in lead halide perovskite nanocrystals," J. Phys. Chem. C **121**(24), 13381–13390 (2017).

[46] R. Kumar, "A new understanding of luminescence processes in feldspar using novel site-selective spectroscopic techniques," Ph.D. thesis, Technical University of Denmark, 2022.

[47] J. Mooney and P. Kambhampati, "Get the basics right: Jacobian conversion of wavelength and energy scales for quantitative analysis of emission spectra," J. Phys. Chem. Lett. **4**(19), 3316–3318 (2013).

[48] D. Hong, Y. Zhou, S. Wan, X. Hu, D. Xie, and Y. Tian, "Nature of photoinduced quenching traps in methylammonium lead triiodide perovskite revealed by reversible photoluminescence decline," ACS Photonics **5**(5), 2034–2043 (2018).

[49] S. Chen, X. Wen, S. Huang, F. Huang, Y. B. Cheng, M. Green, and A. Ho-Baillie, "Light illumination induced photoluminescence enhancement and quenching in lead halide perovskite," Solar RRL **1**(1), 1–8 (2017).

[50] A. Xie, T. H. Nguyen, C. Hettiarachchi, M. E. Witkowski, W. Drozdowski, M. D. Birowosuto, H. Wang, and C. Dang, "Thermal quenching and dose studies of x-ray luminescence in single crystals of halide perovskites," J. Phys. Chem. C **122**(28), 16265–16273 (2018).

[51] N. Onoda-Yamamuro, T. Matsuo, and H. Suga, "Dielectric study of $CH_3NH_3PbX_3$ ($X = Cl, Br, I$)," J. Phys. Chem. Solids **53**(7), 935–939 (1992).

[52] X. Zhang, S. Zhu, Y. Li, Y. Zhan, X. Chen, F. Kang, J. Wang, and X. Cao, "Gamma rays excited radioluminescence tomographic imaging," Biomed. Eng. Online **17**(1), 45 (2018).

[53] A. N. Belsky, N. A. Fedorov, I. A. Frolov, I. A. Kamenskikh, P. Martin, E. D. Rubtsova, I. N. Shpinkov, D. A. Spassky, A. N. Vasil'ev, and B. I. Zadneprovsky, "Excitation density effects in the luminescence yield and kinetics of $MAPbBr_3$ single crystals," Crystals **13**(7), 1142 (2023).

[54] G. Kitis, J. M. Gomez-Ros, and J. W. N. Tuyn, "Thermoluminescence glow-curve deconvolution functions for first, second and general orders of kinetics," J. Phys. D: Appl. Phys. **31**(19), 2636 (1998).

[55] A. Pisoni, J. Jaćimović, O. S. Barišić, M. Spina, R. Gaál, L. Forró, and E. Horváth, "Ultra-low thermal conductivity in organic–inorganic hybrid perovskite CH_3 NH_3 PbI_3," J. Phys. Chem. Lett. **5**(14), 2488–2492 (2014).

[56] S. A. Moiz, I. A. Khan, W. A. Younis, and K. S. Karimov, "Space charge–limited current model for polymers," Conduct. Polym. **5**, 91 (2016).

[57] P. Wiśniewski and B. Majkusiak, "Charge-trapping-induced hysteresis effects in highly doped silicon metal–oxide–semiconductor structures," Materials **15**(8), 2733 (2022).

[58] J. M. Burst, J. N. Duenow, D. S. Albin, E. Colegrove, M. O. Reese, J. A. Aguiar, C. S. Jiang, M. K. Patel, M. M. Al-Jassim, D. Kuciauskas, S. Swain, T. Ablekim, K. G. Lynn, and W. K. Metzger, "CdTe solar cells with open-circuit voltage breaking the 1 V barrier," Nat. Energy **1**(4), 1–8 (2016).

[59] S. De Wolf, J. Holovsky, S. J. Moon, P. Löper, B. Niesen, M. Ledinsky, F. J. Haug, J. H. Yum, and C. Ballif, "Organometallic halide perovskites: Sharp optical absorption edge and its relation to photovoltaic performance," J. Phys. Chem. Lett. **5**(6), 1035–1039 (2014).

[60] Z. Ni, C. Bao, Y. Liu, Q. Jiang, W.-Q. Wu, S. Chen, X. Dai, B. Chen, B. Hartweg, Z. Yu, Z. Holman, and J. Huang, "Resolving spatial and energetic distributions of trap states in metal halide perovskite solar cells," Science **367**(6484), 1352–1358 (2020).

[61] X. Lao, Z. Yang, Z. Su, Z. Wang, H. Ye, M. Wang, X. Yao, and S. Xu, "Luminescence and thermal behaviors of free and trapped excitons in cesium lead halide perovskite nanosheets," Nanoscale **10**(21), 9949–9956 (2018).